The Astrophysical Journal Letters, 1005:L50 (9pp), 2026 July 10 https://doi.org/10.3847/2041-8213/ae7d2e

Validation of an Extreme-ultraviolet Desaturation Technique for the Atmospheric Imaging Assembly on Board the Solar Dynamics Observatory Using Observations from the Extreme Ultraviolet Imager on Board Solar Orbiter

Sabrina Guastavino[1,2], David Berghmans[3], Cis Verbeeck[3], Stefan J. Hofmeister[4], Emil Kraaikamp[3], Ewan C. M. Dickson[3], Federico Benvenuto[1], Paolo Massa[5], Anna Maria Massone[1,2], and Michele Piana[1,2]
[1] MIDA, Dipartimento di Matematica, Università di Genova, Via Dodecaneso 35, I-16146 Genoa, Italy; sabrina.guastavino@unige.it
[2] Osservatorio Astrofisico di Torino, Istituto Nazionale di Astrofisica, via Osservatorio 20, I-10025 Pino Torinese, Italy
[3] Solar-Terrestrial Centre of Excellence - SIDC, Royal Observatory of Belgium, Ringlaan 3 Avenue Circulaire, B-1180 Brussels, Belgium
[4] Columbia Astrophysics Laboratory, Columbia University, NY, USA
[5] University of Applied Sciences and Arts Northwest Switzerland (FHNW), School of Computer Science, Bahnhofstrasse 6, Windisch 5210, Switzerland
Received 2026 June 11; accepted 2026 June 15; published 2026 July 2

Abstract

High-dynamic-range imaging in the extreme-ultraviolet regime is frequently compromised by detector saturation and charge blooming during intense solar flares, preventing reliable photometry of flare cores. This study presents, for the first time, a direct validation of a sparsity-regularized inverse-diffraction desaturation algorithm applied to saturated images from the Atmospheric Imaging Assembly on the Solar Dynamics Observatory, using contemporaneous short-exposure, unsaturated observations from the Extreme Ultraviolet Imager on Solar Orbiter. The validation exploits a near-radial spacecraft alignment on 2024 March 19, when an M2.1 flare erupted in active region 13615. To obtain coregistered intensity maps, the data were processed with reprojection onto a common helioprojective grid, exposure-time normalization, light-travel-time correction, and field-of-view pointing refinement. Photometric comparisons were performed using peak-based statistics within a rigorously defined region of interest. Results show close morphological agreement and a temporally stable ratio between the desaturated and reference intensities through the impulsive and early decay phases. An early-phase discrepancy is observed and attributed to rapid subexposure evolution, sampling effects, and bandpass/response differences. These findings demonstrate that the desaturation procedure successfully recovers physically meaningful time-dependent core fluxes and, for the first time, provide independent empirical support for the use of desaturated archive frames in quantitative studies of large flares.

Unified Astronomy Thesaurus concepts: Solar flares (1496); Astronomy image processing (2306); Solar extreme ultraviolet emission (1493); Astronomy data analysis (1858); Computational methods (1965)

Materials only available in the online version of record: animation

1. Introduction

High-cadence, full-disk extreme-ultraviolet (EUV) imaging has transformed the empirical view of coronal dynamics and flaring energy release. Since its launch, the Atmospheric Imaging Assembly (AIA; J. R. Lemen et al. 2012) on board the Solar Dynamics Observatory (SDO; W. D. Pesnell et al. 2012) has provided multiwavelength EUV animations with 1.″5 spatial resolution and 12 s cadence that are widely used to study the temporal and spatial evolution of active regions (ARs), flares, and eruptive phenomena. However, charged coupled device (CCD)–based EUV imaging is intrinsically limited by pixel saturation and charge blooming during intense flares: the brightest core emission overflows the detector wells (primary saturation), and spilled charge contaminates neighboring pixels (blooming), producing large, anisotropic regions of corrupted data and strong diffraction artifacts outside the saturated core. These effects compromise both qualitative interpretation and quantitative photometry of the most energetic events, which are often the most scientifically interesting ones. The saturation problem therefore represents a major obstacle to the routine exploitation of AIA data for the study of large flares.

A pragmatic solution to recover the lost signal in saturated AIA frames is to exploit the information encoded in the diffraction patterns due to the instrument point-spread function (PSF; P. Grigis et al. 2012). Because only part of the incoming photon flux is recorded in saturated pixels while a coherent fraction is scattered into diffraction fringes, the diffraction pattern carries indirect information about the true flux in the primary-saturated core (see, e.g., G. Torre et al. 2015; S. Guastavino et al. 2019; and S. Guastavino & F. Benvenuto 2021, for a detailed description of the AIA-PSF, diffraction artifacts, and the saturation/blooming problem). This inverse-diffraction idea underlies earlier pipelines such as DESAT (G. Torre et al. 2015) and, more recently, the Sparsity-Enhancing DESAT (SE-DESAT) algorithm introduced by S. Guastavino et al. (2019). SE-DESAT frames the recovery as a constrained inverse problem that (i) assumes that the diffraction effects observed in the original image are generated only by a subset of pixels within the saturated region, i.e., the primary-saturated pixels; (ii) enforces an energetic constraint on column-wise counts to preserve the total recorded charge in the saturation area; and (iii) uses a sparsity-enhancing, Poisson-regularized approach called Poisson Reweighted Lasso (PRiL; S. Guastavino & F. Benvenuto 2019) combined

with an alternating expectation–maximization step to estimate simultaneously the background, the segmentation between primary saturation and blooming, and the reconstructed primary-region flux. This approach avoids reliance on external short-exposure time frames temporally near the saturated image in order to have an a priori estimate of the background and can operate on long saturated sequences where interpolation from unsaturated neighbors is impossible (for example, during intense, persistent solar storms). Detailed algorithmic description and tests on synthetic data and AIA observations of the 2017 September event are given in S. Guastavino et al. (2019). An enhanced version, Adaptive SE-DESAT, incorporates spatially dependent weighting in the sparsity term, guided by the morphology of the saturated region, to reduce the occasional artifacts seen in SE-DESAT reconstructions. For full methodological details of Adaptive SE-DESAT and its exploitation of the AIA diffraction pattern to reconstruct primary-saturated flux, the reader is referred to S. Guastavino & F. Benvenuto (2021).

Despite the potentiality of Adaptive SE-DESAT in producing plausible and self-consistent reconstructions, an intrinsic difficulty remains: the absence of a true observational ground truth for saturated pixels. A natural validation strategy is to compare Adaptive SE-DESAT reconstructions of saturated AIA frames with independent, truly unsaturated observations of the same scene. Historically, two approaches have been used. First, AIA itself sometimes records short-exposure frames that do not saturate; these provide an AIA-internal ground truth but are not always available and, when present, are frequently highly noisy because short exposures reduce the signal-to-noise ratio (further, during large flares, also short-exposure frames can be saturated). Second, simulations and synthetic tests can quantify algorithmic performance under controlled conditions but cannot replace measurement-based validation. The combination of these limitations motivated the search for an independent instrument that (i) observes the same EUV passband (or a closely comparable one); (ii) provides high-resolution, short-exposure, unsaturated imagery of flaring cores; and (iii) can be registered to AIA with sufficient geometric and radiometric fidelity to permit quantitative comparison.

The launch and commissioning of the ESA/NASA Solar Orbiter mission (D. Müller et al. 2020) and, in particular, its Extreme Ultraviolet Imager (EUI; P. Rochus et al. 2020), created precisely this validation opportunity. EUI consists of a Full Sun Imager (FSI) and two High Resolution Imagers (HRIs). FSI and HRIEUV, which is one of the HRI telescopes, both observe at 17.4 nm, which closely matches the coronal 17.1 nm passband used by AIA. HRIEUV provides high spatial resolution (2 pixel resolution $\approx 1''$) on a 2048×2048 detector and is capable of short-exposure times and high cadence, making it well suited to record flare cores without saturation while retaining good signal-to-noise ratio in short exposures. The EUI instrument design, spectral response, and resolution are described in detail in the EUI instrument paper (P. Rochus et al. 2020); the HRIEUV channel is thus particularly suited for joint science with AIA-like channels and for synergy in cross-calibration and high-resolution studies.

A particularly favorable geometric condition for direct instrument cross validation occurs during radial alignments between Solar Orbiter and SDO. In a radial alignment, the two spacecraft, the Sun, and, specifically, the target AR become approximately collinear so that the line-of-sight directions are nearly the same and both imagers view essentially the same solar hemisphere with a very small parallax of disk features. Under these circumstances, the projected solar disk and the local fields of view of AIA and EUI/FSI overlap to a high degree; differences in apparent feature location reduce to small reprojection shifts that can be handled by standard World Coordinate System (WCS) remapping and reprojection techniques. Because Solar Orbiter is typically closer to the Sun, the EUI/HRIEUV images naturally have different a geometric scale and higher intrinsic angular resolution, but these differences are systematic and quantifiable: EUI frames can be remapped onto AIA geometry (or vice versa) and radiometrically scaled, taking into account measured instrument responses and exposure times. Hence, radial alignments provide an observational configuration in which EUI/HRIEUV short-exposure, unsaturated images serve as an independent empirical reference for validating Adaptive SE-DESAT reconstructions of saturated AIA frames.

On 2024 March 19, Solar Orbiter and SDO were in a favorable radial alignment, being only about 1° apart in heliographic longitude, while Solar Orbiter was near 0.44 au from the Sun. During that interval, an M2.1 flare erupted from NOAA AR 13615 (D. F. Ryan et al. 2025). AIA frames of the event showed strong saturation and blooming in the flare core, whereas EUI/HRIEUV observations taken with short exposure times remained unsaturated and recorded the same emitting region at high spatial resolution. This unique coincidence enables, for the first time, a direct, spatially resolved and quantitative validation of Adaptive SE-DESAT against genuinely independent measurements: by carefully reprojecting and coregistering EUI/HRIEUV frames to AIA geometry, one can compare the Adaptive SE-DESAT reconstructed AIA core intensities with the independently measured EUI intensities on a pixel-by-pixel basis. In the analysis presented here, this strategy is adopted to demonstrate that, after Adaptive SE-DESAT desaturation, there is morphological agreement in the reconstruction of the most intense regions. Additionally, the ratio of AIA to EUI/HRIEUV time series in the flare core is approximately constant over the peak and early decay phases of the event, strongly supporting the hypothesis that Adaptive SE-DESAT recovers physically meaningful photon fluxes in the primary-saturated region.

The scientific and practical implications of a successful validation are substantial. If Adaptive SE-DESAT provides quantitatively reliable reconstructions, then the entire AIA archive of saturated flare frames, formerly suspect for photometric studies, can be exploited for flare energetics, timing, and morphology with confidence after desaturation. This increases the usable sample of intense flares by orders of magnitude and removes a systematic data gap that has limited statistical and case studies of the most powerful solar events.

This Letter documents the validation experiment and its results. Section 2 describes the AIA and EUI datasets, exposure histories, and the reprojection and radiometric corrections applied; Section 3 details the quantitative comparison methodology, including coregistration, resolution matching, and the statistical metrics used to compare time series and spatial patterns; Section 4 presents the main validation results, including pixel-level comparisons; and Section 5 discusses implications and limitations (including instrumental and line-

formation differences that can bias direct comparisons). Our conclusions are offered in Section 6, together with an outline of recommended next steps for broader applications of Adaptive SE-DESAT across the AIA archive.

2. AIA and EUI Data

The validation experiment employs AIA and EUI simultaneous EUV observations of the M2.1 flare that originated in NOAA AR 13615 on 2024 March 19. The flare onset at the Sun occurred at 23: 17 UT, reached peak emission at 23: 27 UT, and declined to near-background levels by 23: 32 UT. A time window of approximately 10 minutes centered on the impulsive phase was selected so as to capture the rapid evolution of the flare core. More specifically, the comparison dataset comprises (i) SDO/AIA 171 Å frames (original, saturated images and their Adaptive SE-DESAT desaturated reconstructions) and (ii) Solar Orbiter/EUI/HRIEUV short-exposure, level-2 images that remain unsaturated in the flare core. We point out that during this flare, also the HRIEUV regular-exposure time images are saturated, so that they cannot be used to validate Adaptive SE-DESAT.

The radial-alignment geometry between Solar Orbiter and SDO during the observation interval provided the observational basis for a direct, spatially resolved cross-instrument validation. At 23: 30 UT on 2024 March 19, the two spacecraft were indeed separated by approximately 1° in heliographic longitude, with Solar Orbiter at ∼0.44 au from the Sun and SDO orbiting around Earth. This orbital configuration resulted in the line of sight to NOAA AR 13615 being effectively common to both instruments, producing a high degree of projected overlap between the AIA and EUI fields of view. More specifically, it minimizes parallax-induced displacement of disk features and reduces reprojection ambiguity: after accounting for the known geometric scale difference and light-travel-time offset, EUI/HRIEUV short-exposure frames can be reprojected onto the AIA helioprojective grid with negligible residual misregistration at the spatial scales relevant for the present comparison. This will be treated explicitly in Section 3. Figure 1 illustrates the relative Sun-spacecraft geometry at the time of interest and highlights the small angular offset and the difference in heliocentric distance.

The AIA observations analyzed in this study correspond to level-1 images in the 171 Å channel, extracted as a 499 × 499 pixel cutout centered on NOAA AR 13615. Each exposure integrates over approximately 2 s, yielding the nominal high-cadence (12 s) temporal sampling characteristic of AIA. The images have an angular scale of $0\farcs6\,\mathrm{pixel}^{-1}$, corresponding to a spatial resolution of about $1\farcs5$, and are recorded in helioprojective-tangent WCS coordinates suitable for direct geometric registration with other solar imagers. The selected AIA frames exhibit pronounced primary saturation and charge blooming within and around the flare core, significantly compromising direct photometry of the brightest regions. For this reason, the Adaptive SE-DESAT algorithm was applied to reconstruct the flux distribution in the saturated region, producing desaturated frames that can be meaningfully compared with independent, unsaturated measurements from Solar Orbiter/EUI. The 171 Å passband, dominated by Fe IX and Fe X emission, matches well the spectral response of the EUI/HRIEUV 174 Å channel (S. V. Shestov et al. 2025), allowing for a physically consistent cross-instrument comparison.

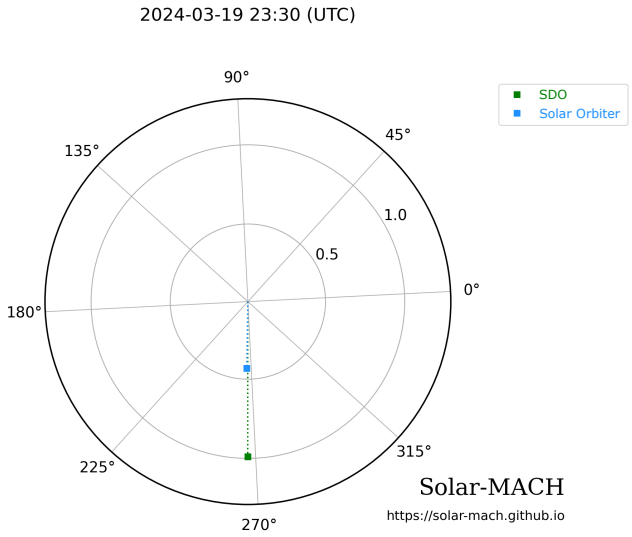

Figure 1. Relative Sun-spacecraft geometry at 23: 30 UT on 2024 March 19. The polar plot (J. Gieseler et al. 2023) shows the positions of SDO (green marker) and Solar Orbiter (blue marker) in heliocentric inertial coordinates projected onto the orbital plane; radial distance is in astronomical units. At the time shown, Solar Orbiter was at 0.435 au, and the longitudinal separation from SDO was ∼1°, producing a near-radial alignment that enables direct, low-parallax comparisons between AIA and EUI images.

The EUI dataset employed (E. Kraaikamp et al. 2023) in the present work comprises level-2 HRIEUV short-exposure frames with an effective exposure time of 0.04 s, an angular sampling of $0\farcs492\,\mathrm{pixel}^{-1}$ on a 2048 × 2048 detector window, and a nominal central wavelength near 174 Å (instrument sensitivity spanning roughly from 171 to 178 Å). The images are delivered in physical units of DN s^{-1} after on-ground radiometric corrections and explicit normalization by integration time. The different heliocentric distances of SDO and Solar Orbiter introduce a systematic geometric scale difference between AIA and EUI, which will be corrected through WCS-based reprojection in Section 3 to enable a direct comparison between the two instruments. The HRIEUV short-exposure frames remain unsaturated in the flare core, provide higher intrinsic spatial fidelity than AIA at the time of observation, and therefore constitute an independent, high-resolution photometric reference for validating desaturation reconstructions. Further details on instrument design and performance are given in the EUI instrument paper (P. Rochus et al. 2020).

Figure 2 shows a direct visual comparison between the original, saturated SDO/AIA 171 Å cutout and the Solar Orbiter/EUI/HRIEUV short-exposure frame, both corresponding to the same solar flare scene that occurred on the Sun at 23: 16: 39 UT on 2024 March 19, (the AIA and EUI frames were actually acquired at 23: 24: 57 UT and 23: 20: 16 UT, respectively, the difference reflecting the distinct light-travel times from the Sun to each spacecraft at 1 and 0.435 au). The left panel displays the 499 × 499 AIA cutout centered on NOAA AR 13615, exhibiting severe primary saturation and charge blooming in the flare core. The right panel visualizes the EUI/HRIEUV short-exposure image of the same region (the AIA field of view is indicated by a cyan square), which remains unsaturated and preserves high spatial fidelity. Note that, to conserve telemetry, the HRIEUV image was clipped at low intensities and only pixel values with high flare intensities were transmitted.

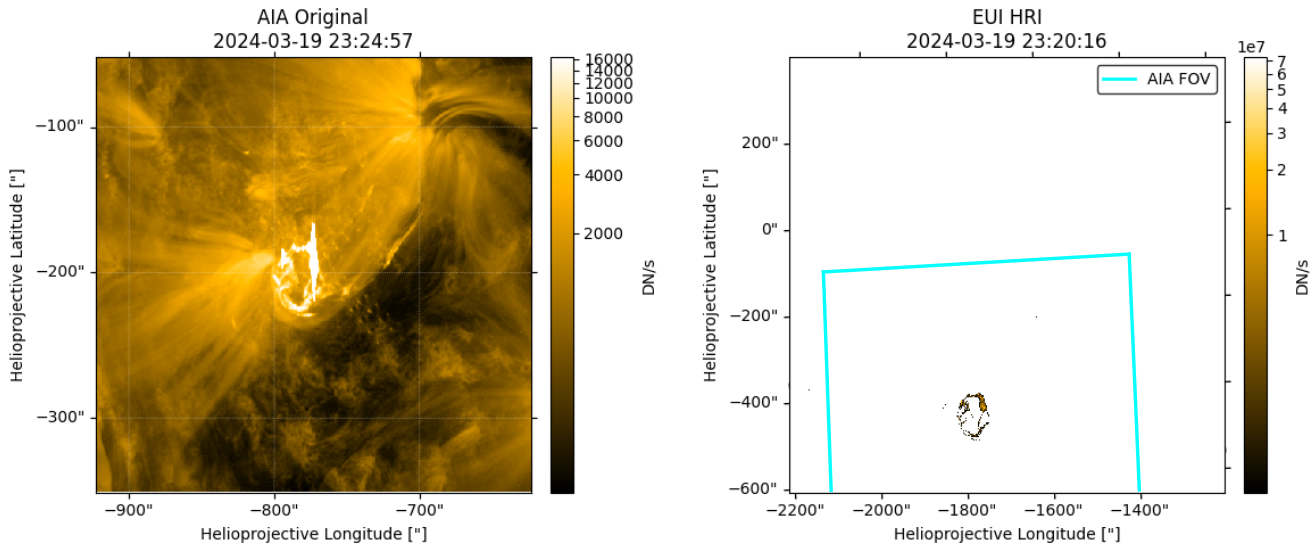

Figure 2. Comparison between SDO/AIA 171 Å and Solar Orbiter/EUI/HRIEUV views of the same solar flare scene on the Sun at 23: 16: 39 UT on 2024 March 19. Left: AIA 171 Å cutout (499 × 499 pixels) acquired at 23: 24: 57 UT showing strong primary saturation and blooming. Right: unsaturated EUI/HRIEUV short-exposure image acquired at 23: 20: 16 UT, with the AIA field of view outlined by a cyan square.

3. Adaptive SE-DESAT Reconstruction Process

This section describes the preprocessing pipeline that produces directly comparable AIA and EUI maps for pixel-by-pixel validation of the Adaptive SE-DESAT reconstructions. The objective is to test whether the desaturated AIA frames reproduce the morphology and intensity evolution recorded independently by unsaturated high-resolution EUI/HRIEUV short-exposure images. The following steps are applied in sequence: exposure-time normalization, EUI pointing adjustment (based on EUI/FSI full solar disk observations), light-travel-time alignment to a common solar-emission reference, and WCS-based reprojection onto a common helioprojective grid.

All photometric comparisons with EUI data are performed using the AIA images that were processed by Adaptive SE-DESAT to reconstruct flux in pixels affected by primary saturation and blooming. To ensure a robust comparative analysis, the two datasets must first be aligned temporally and normalized to account for their different exposure times and acquisition geometries. Both the original and desaturated AIA frames are therefore converted to units of DN s^{-1} by normalizing the recorded counts by the exposure time. While this does not place them on an absolute radiometric scale, it makes their observed intensities comparable with those of the EUI/HRIEUV level-2 products.

Coregistration between AIA and EUI/HRIEUV is optimized through a small pointing refinement of the HRIEUV data, using EUI/FSI observations as an intermediate reference. Because FSI provides a larger field of view, it can be aligned to AIA through standard limb-fitting procedures. However, the accuracy of this limb fit is inherently constrained by the lower spatial resolution of FSI. Consequently, the residual reprojection uncertainty is estimated to be on the order of $\sim 1''$. Once FSI is registered to AIA, the same geometric correction is transferred to the narrower HRIEUV to reduce off-pointing and improve the fidelity of subsequent reprojection. The correction is applied at the WCS level so that the corrected HRIEUV product carries updated reference coordinates and can then be used for all further resampling. While this FSI-driven adjustment cannot yield subarcsecond precision, it effectively mitigates larger pointing biases that would otherwise contaminate the pixelwise comparison and is particularly useful when HRIEUV narrow-field imagery cannot be reliably cross-matched directly to AIA because of scale and resolution differences.

Temporal alignment between EUI and AIA is performed by referencing all images to the same solar-emission instant rather than to their spacecraft acquisition times. Differences in spacecraft–Sun distance produce measurable light-travel-time offsets. During the radial alignment considered here, Solar Orbiter was significantly closer to the Sun than SDO, so onboard timestamps are corrected by the light-travel delay appropriate to each spacecraft. Registering all frames to a common solar-referenced time ensures that the compared maps capture the same physical scene on the Sun, thereby preventing artificial apparent motion in rapidly evolving flare structures. In doing so, most of the short-exposure-time EUI/HRIEUV images fall within the interval of the acquisition time of the corresponding AIA images or have a time offset of no more than half of the AIA exposure time, i.e., 1 s.

A direct morphological comparison requires spatially reprojecting the AIA and EUI/HRIEUV images onto a common helioprojective grid. The HRIEUV observations are therefore resampled onto the AIA reference geometry. The target grid is defined by the WCS of the desaturated AIA map, ensuring that all subsequent comparisons are performed at the native AIA pixel sampling. The reprojection is carried out conservatively with respect to photometric flux: resampling methods that preserve the total integrated intensity across pixels are employed to minimize artificial smoothing and maintain radiometric consistency when changing pixel scale.

The residual differences in spatial resolution between AIA and EUI/HRIEUV are negligible for the spatial scales of the regions analyzed in this work. As a result, the two spatially and temporally aligned datasets are directly suitable for pixel-by-pixel comparison.

Although radiometric cross calibration between instruments is not addressed in the present study (e.g., by empirically

estimating an interinstrument multiplicative scale factor from stable, cospatial quiet peripheral regions or from pre-/postflare intervals when saturation is absent), the principal validation diagnostic remains the temporal constancy of the ratio between the desaturated AIA and EUI/HRIEUV intensities in the flaring site. If Adaptive SE-DESAT accurately recovers the saturated flux, this ratio should remain approximately constant during the impulsive and early decay phases of the flare, irrespective of any absolute photometric scale alignment, whereas deviations from constancy reveal limitations in the desaturation reconstruction.

A region of interest (ROI) surrounding the flare core is selected on the AIA desaturated map to focus the analysis on the portion of the image most impacted by saturation and to ensure that the photometric comparison with EUI/HRIEUV data is spatially consistent. This selected region is then propagated to all aligned products so that statistics are computed on strictly cospatial pixels.

Within this masked ROI, peak-based measures obtained by identifying the top three, tp five, and tp eight brightest valid pixels are computed for each frame. We point out that the number eight is motivated by the fact that it represents the maximum number of available pixels for the entire temporal range of the analysis (from 23:23:45 to 23:34:57 UT). The coordinates of the brightest EUI/HRIEUV pixels are used to sample AIA and desaturated AIA values at the same locations to assess a local, high-signal test of photometric agreement. More specifically, the validation strategy is twofold. Morphological similarity is assessed qualitatively by comparing spatial structures in the desaturated AIA and the reprojected EUI/HRIEUV maps, overplotting one image over the other to assess similarity of shape and location in the flaring site. Photometric agreement is quantified by the approximate temporal stability of the ratio of desaturated AIA to EUI intensity in the ROI throughout the impulsive and early decay flare phases. Together, this observational evidence constitutes the first direct, image-based, cross-instrument confirmation that scientifically meaningful fluxes in pixels affected by primary saturation can be recovered by means of a computational process. The results of this validation procedure are reported in Section 4.

4. Results

Figures 3 and 4 provide a detailed visual comparison of the flaring region as captured by EUI and the corresponding desaturated AIA images, serving as the basis for the validation of Adaptive SE-DESAT reconstructions. A zoomed-in view of the event is shown, corresponding to the solar scene at 23: 16: 39 (23: 21: 53) UT on 2024 March 19; the AIA image was acquired at 23: 24: 57 (23: 30: 09) UT and the EUI/HRIEUV frame was acquired at 23: 20: 16 (23: 25: 30) UT, after accounting for light-travel-time differences. In the top-left panel, the original AIA image clearly exhibits a saturated core region where the detector wells are clipped, resulting in primary saturation, while excess charge spreads into neighboring pixels along characteristic (vertical) directions, producing blooming. The top-right panel illustrates the output of the Adaptive SE-DESAT algorithm applied to the same frame. Here, the previously saturated region is reconstructed, displaying a smooth and coherent intensity pattern that restores a physically plausible spatial structure. The bottom-left panel presents the independently acquired EUI/HRIEUV short-exposure frame, which remains unsaturated and captures the same flaring region. This panel serves as a reference for both morphology and intensity distribution, providing an empirical basis to evaluate the desaturated AIA data. In the bottom-right panel, the overlay of the reprojected EUI/HRIEUV frame and the desaturated AIA image demonstrates the remarkable agreement between the two products.

In both cases, the spatial pattern of emission in the flare core, including the relative placement of substructures and regions of enhanced intensity, closely matches between the desaturated AIA and the EUI/HRIEUV observations. The reconstructed AIA image is not only morphologically consistent with EUI, but it also reproduces the spatial variation in intensity, suggesting that the desaturation process captures the underlying flux distribution. While visual inspection alone cannot replace rigorous quantitative validation, this figure offers an immediate and compelling summary of the algorithm's performance. This morphological agreement complements the pixel-by-pixel analyses, whose results are presented below, showing the temporal evolution of the flare in the desaturated AIA series compared with the unsaturated EUI observations to assess the stability of the reconstructed flux over the impulsive and early decay phases of the flare.

Figures 5 summarizes the pixel-by-pixel photometric comparisons between the reprojected EUI/HRIEUV short-exposure images and both the original (saturated) AIA frames and the Adaptive SE-DESAT desaturated reconstructions. We consider the intersection between the HRIEUV mask and the AIA estimated primary saturation mask and we make the analysis on the three, five, and eight most intense pixels of HRIEUV images in this intersection mask. The top row of Figure 5 displays the light curves formed by summing the three, five, and eight brightest valid pixels, respectively, in this mask. Three curves are shown in each panel: the reprojected EUI/HRIEUV signal (red), the original AIA signal (green), and the Adaptive SE-DESAT desaturated AIA signal (blue), all sampled at the same coordinates. The time series are expressed in DN s^{-1} (counts normalized by exposure time) to remove trivial exposure-time differences between instruments. In these panels, the EUI/HRIEUV light curve has been rescaled by 10^{-2} to facilitate visual comparison with the AIA curves, though it is not used in any quantitative calculations. The bottom panels of Figure 5 show the time series of the ratio between the HRIEUV signal and AIA original (green) and desaturated (blue) light curves. Incidentally, all interinstrument ratios displayed in Figure 5 are estimated from the original (unscaled) DN s^{-1} values for both instruments.

Two main empirical results emerge from these plots. First, the morphological and temporal coherence between EUI/HRIEUV and the Adaptive SE-DESAT reconstructions is substantially improved relative to the original saturated AIA frames. In particular, the blue (desaturated AIA) curve closely tracks the red (EUI/HRIEUV) curve across the impulsive and early decay phases: both the timing and the shape of the main impulsive peak and of the subsequent decay are fairly well reproduced. By contrast, the original AIA (green) curve is flat due to saturation. Second, this improvement is clearly quantified by the interinstrument ratios plotted in the bottom row of Figure 5. The ratio with the original AIA displays dramatic, rapid variations during the impulsive phase, consistent with the expected loss of linear photometry in saturated pixels. By contrast, the ratio with the desaturated

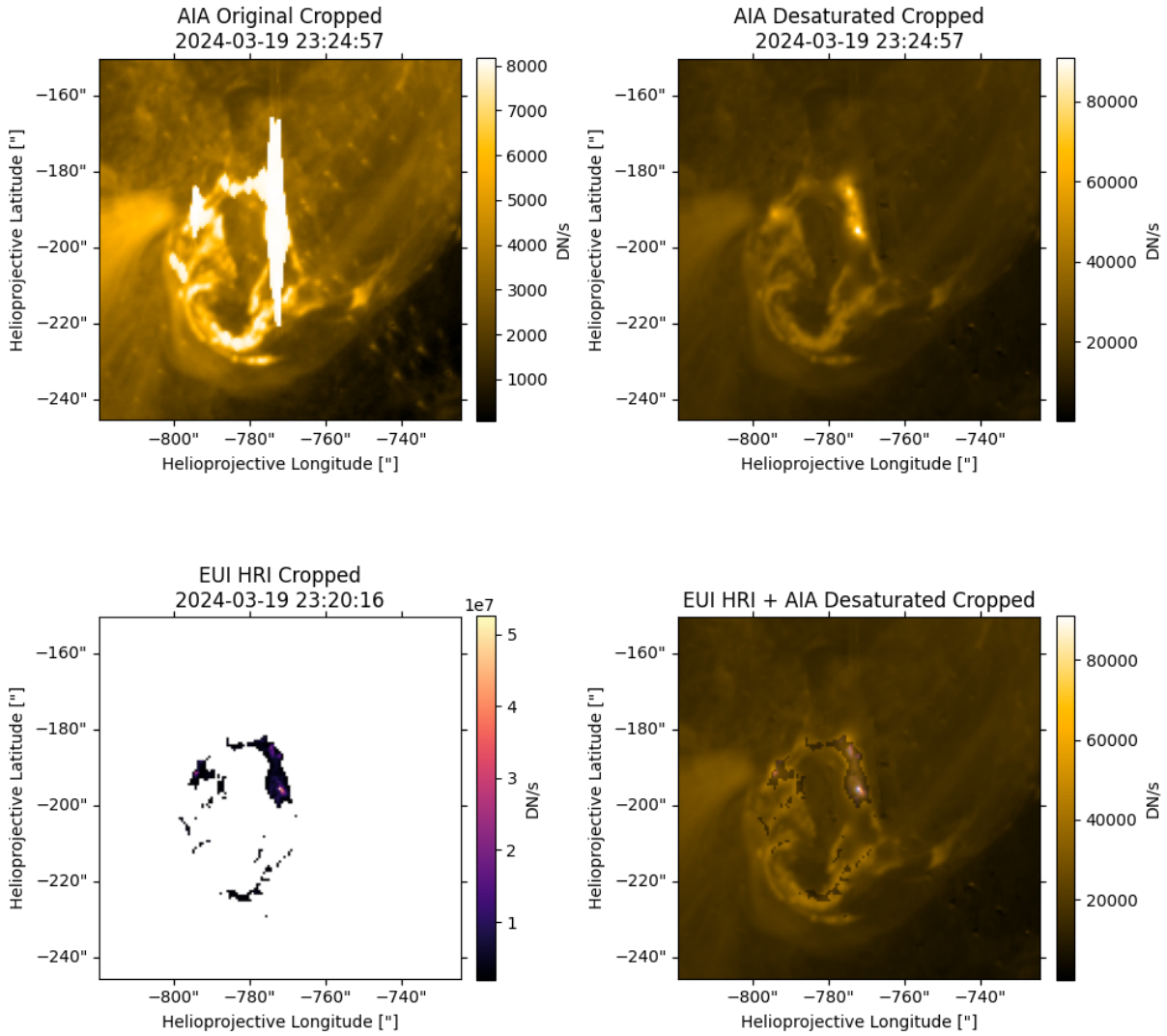

Figure 3. Zoomed-in crop of the flaring site on 2024 March 19, at a solar-referenced time of 23: 16: 39 UT. Top left: original SDO/AIA 171 Å image. Top right: same AIA frame after desaturation with Adaptive SE-DESAT. Note that the reconstructed flaring region has values well beyond the AIA instrumental dynamic range. Bottom left: Solar Orbiter/EUI/HRIEUV short-exposure image. Bottom-right: overlay of the reprojected EUI/HRIEUV image and the desaturated AIA frame, illustrating close spatial and morphological correspondence. The original AIA and EUI frames were acquired at 23: 24: 57 UT and 23: 20: 16 UT, respectively, and have been corrected for light-travel time and reprojected to a common helioprojective grid. A time-sequence animation during the flare event is available.

(An animation of this figure is available in the online article.)

AIA converges to an approximately constant value after the flare peak. More specifically, after ≈23: 27 UT, the EUI/HRIEUV-AIA (desaturated) ratio remains essentially constant in time, for the top three, top five, and top eight statistics. This temporal constancy is precisely the behavior predicted for a successful desaturation algorithm: once the saturated core flux is correctly recovered (up to an overall multiplicative interinstrument calibration factor), the relative photometry between instruments should be stable while the source evolves.

5. Discussion

Taken together, the previous results provide strong empirical support for the photometric fidelity of Adaptive SE-DESAT for this event. The algorithm reconstructs a time history of core intensities that is consistent with independent, unsaturated EUI/HRIEUV measurements to within a nearly constant multiplicative factor throughout the impulsive and early decay phases. Because the EUI/HRIEUV frames at short-exposure time remain unsaturated and were processed to DN s^{-1} on a per-exposure basis, the observed temporal constancy of the ratio demonstrates that Adaptive SE-DESAT recovers the relative photon-flux evolution accurately, i.e., that the desaturated AIA frames preserve the true time dependence of the core emission. A residual mismatch, however, persists during the earliest portion of the impulsive phase (before ≈23: 27 UT); these deviations appear for all the three analyses, though their amplitude is larger for the top three statistic (which, since it refers to a smaller number of highest-signal pixels, is therefore more sensitive to single-pixel modeling errors or localized reprojection offsets).

This mismatch likely arises from multiple, partly overlapping effects, including (i) rapid subexposure evolution and timing mismatch; (ii) the presence of multiple spatially distributed saturated regions during the earliest impulsive

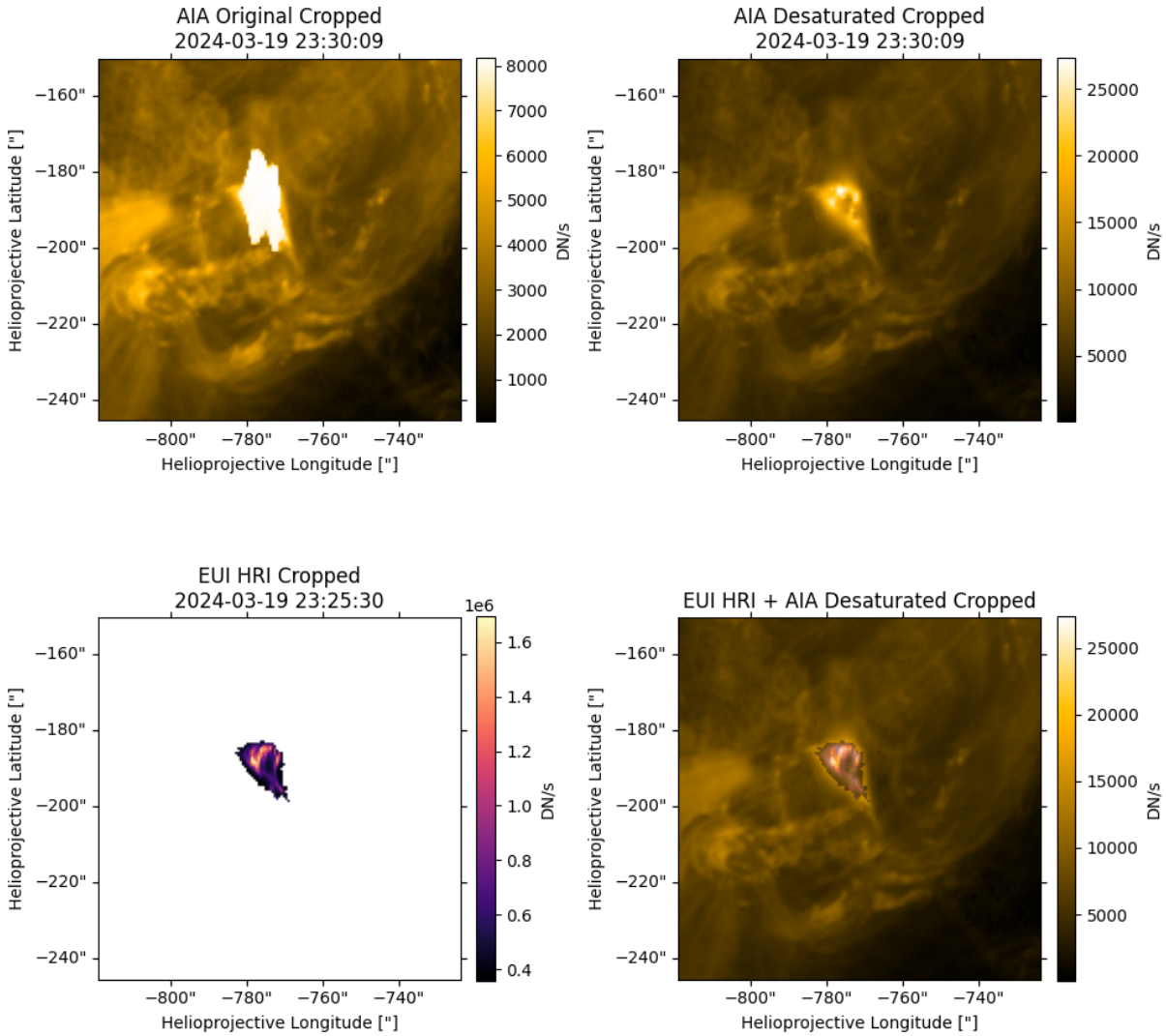

Figure 4. Same as Figure 3, but for a solar-referenced time of 23: 21: 53 UT.

phase, which can lead to a partial loss of fringe information; (iii) residual reprojection and sampling effects; and (iv) radiometric cross-calibration differences. More specifically, even after light-travel correction, the effective solar-referenced times of EUI and AIA exposures do not coincide exactly because of differences in cadence and exposure centroids; during the most rapid brightness changes, this timing offset can produce appreciable deviations in instantaneous ratios. Then, in the earliest impulsive phases of the flaring event, when solar activity is high, the fringes generated by saturated pixels can fall into other saturated regions. As a result, this information is lost and thus cannot be used in the diffraction inverse problem, leading to an underestimation of the primary area. Furthermore, residual reprojection and resampling effects between HRIEUV and the AIA grid may represent a major contribution to the observed mismatch. While integrated flux is conserved, the signal is redistributed across pixels. During the earliest impulsive phase, when the flaring emission is highly compact and evolves rapidly, even small residual coalignment errors or sampling differences can prevent the brightest EUI and AIA pixels from corresponding exactly, leading to systematic biases in point-wise comparisons. As the emitting region expands spatially, the impact of these effects is expected to decrease. Finally, modest passband differences (171 Å compared to the nominal 174 Å channel response function) can induce the observation of partially different flaring morphology if the plasma thermal structure evolves during the impulsive onset.

Despite this residual early-time mismatch, the demonstrated temporal constancy of the EUI/HRIEUV-AIA (desaturated) ratio during and after the impulsive peak is compelling evidence that Adaptive SE-DESAT reconstructs physically meaningful fluxes in primary-saturated pixels for this event. Practically, this result implies that scientifically valuable photometry (timing, energetics, and relative intensity evolution) of saturated AIA cores can be recovered by Adaptive SE-DESAT, subject to an overall interinstrument multiplicative scale factor that can be obtained by independent cross calibration. This substantially increases the utility of AIA for studies of large flares where saturation previously prevented reliable photometric analysis and has several important scientific consequences. First, assuming a high level of intensity accuracy, robust desaturation enables the application of differential emission measure (DEM) techniques to flare cores that previously were unavailable to quantitative DEM inversion because of severe saturation. With temporally

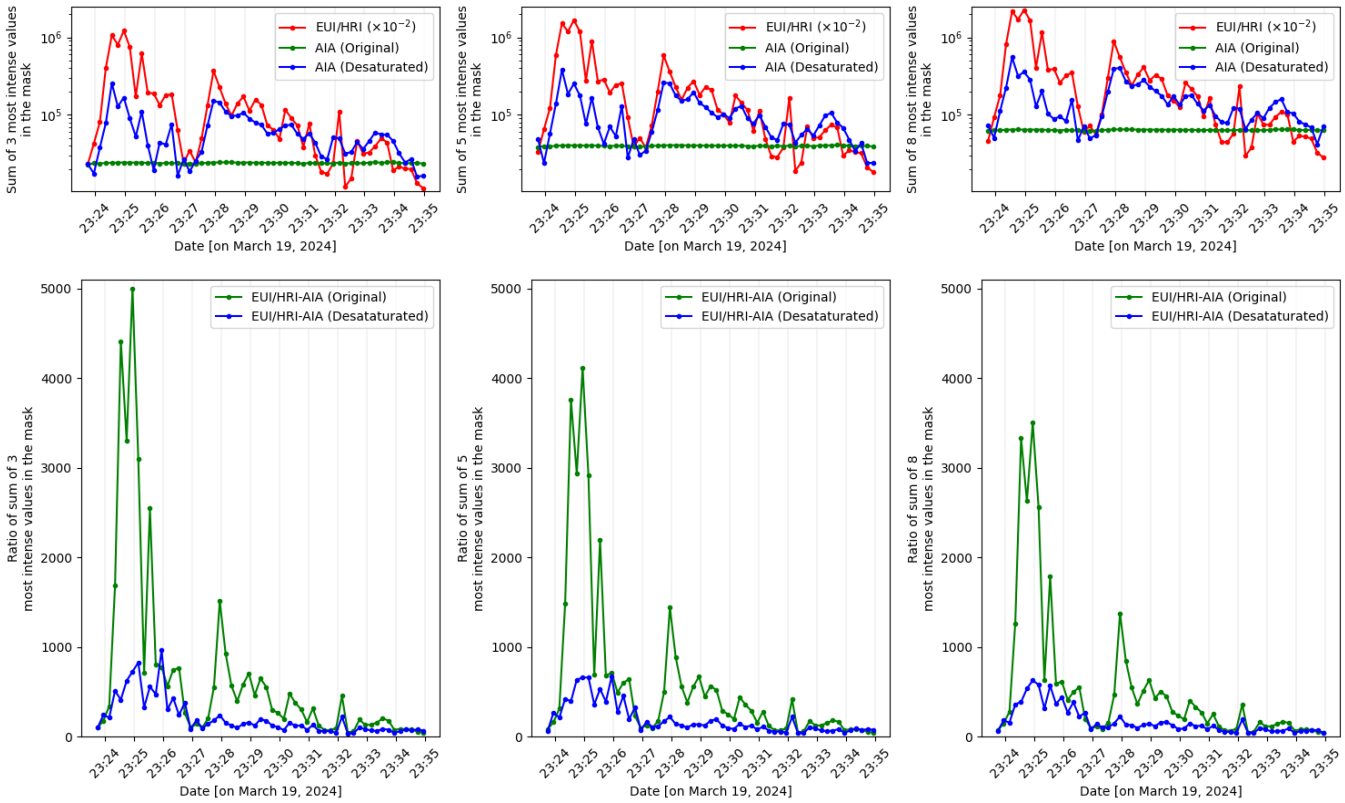

Figure 5. Pixel-level light curves at the intersection between the EUI/HRIEUV validity mask and the AIA estimated primary-saturated mask. Top row: from left to right, time series of the sum of the three, five, and eight brightest pixels for EUI/HRIEUV (graphically rescaled by 10^{-2}, red), AIA original (green), and AIA desaturated (blue). Bottom row: from left to right, time series of the ratio between the sum of the three, five, and eight brightest pixels for EUI/HRIEUV and the corresponding sum of AIA original (green), and AIA desaturated (blue).

resolved, desaturated AIA intensities across different EUV bandpasses, it becomes possible to reconstruct the evolving DEM in the impulsive and early decay phases at spatial scales that include the brightest cores (e.g., P. Massa et al. 2023). This, in turn, allows the tracking of the rapid evolution of plasma temperature and emission measure during energy release, the estimation of the time-dependent thermal energy content of the core, and the investigation of the relationship between heating episodes and the appearance of high-temperature components, analyses that are central to discriminating between heating mechanisms and energy transport models in flares. Second, validated desaturated time series allow improved energetics and timing diagnostics. For example, reliable core photometry permits a direct comparison between EUV radiative signatures and hard X-ray light curves, for instance, with the Spectrometer Telescope for Imaging X-rays (STIX; S. Krucker et al. 2020) on Solar Orbiter, enabling tighter constraints on the timing between thermal and nonthermal energy deposition (M. Piana et al. 2022). Similarly, better recovered peak intensities give more accurate radiative loss estimates and improve integrated energy budgets for individual events and statistical samples.

In summary, although early impulsive-phase discrepancies remain and merit targeted refinement, the present pixel-by-pixel comparison provides the first direct, image-based demonstration using independent, unsaturated EUI/HRIEUV observations, for which Adaptive SE-DESAT produces temporally stable and morphologically consistent reconstructions for the flare core, validating its use for subsequent photometric and morphological studies of such events.

6. Conclusions

A direct, image-based validation of the Adaptive SE-DESAT algorithm, a sparsity-regularized inverse-diffraction desaturation method, has been presented using independent short-exposure observations from the EUI on board Solar Orbiter, obtained during a near-radial alignment with SDO. The selected test case, an M2.1 flare in NOAA AR 13615 on 2024 March 19, provided an unprecedented opportunity to compare reconstructed intensities in primary-saturated regions of AIA 171 Å frames with genuinely unsaturated, high-resolution EUI/HRIEUV measurements. The processing workflow included exposure-time normalization, light-travel-time correction, field-of-view pointing refinement via full-disk imagery, and conservative WCS-based reprojection designed to preserve integrated flux. Photometric validation was performed through peak-sum diagnostics (top three, top five, and top eight brightest valid pixels) within a cospatial ROI.

The principal results are (i) the Adaptive SE-DESAT reconstructions reproduce the fine spatial morphology of the flaring core observed by EUI/HRIEUV; and (ii) the temporal evolution of the reconstructed core intensities closely follows the independent short-exposure reference, with the interinstrument ratio stabilizing to an approximately constant value after the impulsive peak, consistent with faithful recovery of the relative photon-flux evolution. A modest mismatch is detected

during the earliest impulsive instants; plausible explanations include rapid subexposure variability, residual sampling, reprojection biases for compact cores, and wavelength-response differences.

Overall, and for the first time using independent unsaturated imagery, Adaptive SE-DESAT is shown to recover physically meaningful fluxes in pixels affected by primary saturation. This validation significantly strengthens confidence in the quantitative use of desaturated AIA archives for flare timing, energetics, and morphological analyses.

Finally, future studies could benefit from adopting the revised AIA-PSF (S. J. Hofmeister et al. 2025) to evaluate how desaturation, and, in turn, the comparison with EUI, are affected by this model.

Acknowledgments

Solar Orbiter is a space mission of international collaboration between ESA and NASA, operated by ESA. The Royal Observatory of Belgium team thanks the Belgian Federal Science Policy Office (BELSPO) for the provision of financial support in the framework of the PRODEX program of ESA under contract number 4000143743. The EUI instrument was built by CSL, IAS, MPS, MSSL/UCL, PMOD/WRC, ROB, LCF/IO with funding from the Belgian Federal Science Policy Office (BELSPO/PRODEX PEA 4000134088, 4000112292, 4000117262, and 4000134474); the Centre National d'Études Spatiales (CNES); the UK Space Agency (UKSA); the Bundesministerium für Wirtschaft und Energie (BMWi) through Deutsches Zentrum für Luft- und Raumfahrt (DLR); and the Swiss Space Office (SSO). "EUI Data Release 6.0 2023-01" is public and can be freely downloaded from the EUI website (https://www.sidc.be/EUI/data/) and from the Solar Orbiter Archive (http://soar.esac.esa.int/soar/). M.P. and A.M.M. are supported by the "Accordo ASI/INAF Solar Orbiter: Supporto scientifico per la realizzazione degli strumenti Metis, SWA/ DPU e STIX nelle Fasi D-E." M.P. also acknowledges the support of the PRIN PNRR 2022 Project "Inverse Problems in the Imaging Sciences (IPIS)" 2022ANC8HL, cup: D53D23005740006. The research by S. G., F.B., A.M.M., and M.P. was performed within the framework of the MIUR Excellence Department Project awarded to Dipartimento di Matematica, Università di Genova, CUP D33C23001110001. S.G., A.M.M., and M.P. are also grateful to the Gruppo Nazionale per il Calcolo Scientifico - Istituto Nazionale di Alta Matematica (GNCS - INdAM).

ORCID iDs

Sabrina Guastavino https://orcid.org/0000-0001-7047-1148
David Berghmans https://orcid.org/0000-0003-4052-9462
Cis Verbeeck https://orcid.org/0000-0002-5022-4534
Stefan J. Hofmeister https://orcid.org/0000-0001-7662-1960
Emil Kraaikamp https://orcid.org/0000-0002-2265-1803
Ewan C. M. Dickson https://orcid.org/0000-0002-3992-8231
Federico Benvenuto https://orcid.org/0000-0002-4776-0256
Paolo Massa https://orcid.org/0000-0002-0993-1974
Anna Maria Massone https://orcid.org/0000-0003-4966-8864
Michele Piana https://orcid.org/0000-0003-1700-991X

References

Gieseler, J., Dresing, N., Palmroos, C., et al. 2023, FrASS, 9, 384
Grigis, P., Su, Y., & Weber, M. 2012, AIA PSF Characterization and Image Deconvolution 2012-Feb-13, NASA, LMSAL, SAO https://hesperia.gsfc.nasa.gov/ssw/sdo/aia/idl/psf/DOC/psfreport.pdf
Guastavino, S., & Benvenuto, F. 2019, Stat. Comput., 29, 501
Guastavino, S., & Benvenuto, F. 2021, InvPr, 37, 015010
Guastavino, S., Piana, M., Massone, A. M., Schwartz, R., & Benvenuto, F. 2019, ApJ, 882, 109
Hofmeister, S. J., Savin, D. W., & Hahn, M. 2025, ApJS, 278, 8
Kraaikamp, E., Gissot, S., Stegen, K., et al. 2023, SolO/EUI Data Release 6.0 2023-01 doi:10.24414/z818-4163
Krucker, S., Hurford, G. J., Grimm, O., et al. 2020, A&A, 642, A15
Lemen, J. R., Title, A. M., Akin, D. J., et al. 2012, SoPh, 275, 17
Massa, P., Emslie, A. G., Hannah, I. G., & Kontar, E. P. 2023, A&A, 672, A120
Müller, D., St. Cyr, O. C., Zouganelis, I., et al. 2020, A&A, 642, A1
Pesnell, W. D., Thompson, B. J., & Chamberlin, P. C. 2012, SoPh, 275, 3
Piana, M., Emslie, A. G., Massone, A. M., Dennis, B. R., et al. 2022, Hard X-Ray Imaging of Solar Flares (Springer)
Rochus, P., Auchère, F., Berghmans, D., et al. 2020, A&A, 642, A8
Ryan, D. F., Hayes, L. A., Collier, H., et al. 2025, SoPh, 300, 152
Shestov, S. V., Zhukov, A. N., Auchère, F., Berghmans, D., & Loicq, J. 2025, A&A, 699, A7
Torre, G., Schwartz, R. A., Benvenuto, F., Massone, A. M., & Piana, M. 2015, InvPr, 31, 095006